ACS OMEGA

Open Access

http://pubs.acs.org/journal/acsodf

Article

Exploring the Structural Stability of 1T-PdO_2 and the Interface Properties of the 1T-PdO_2/Graphene Heterojunction

Muhammad Yar Khan,* Arzoo Hassan,* Abdus Samad, and Abdullah Al Souwaileh

Cite This: *ACS Omega* 2024, 9, 28176−28185

Read Online

ACCESS | Metrics & More | Article Recommendations

ABSTRACT: Motivated by a recent study on the air stability of $PdSe_2$, which also reports the metastability of the PdO_2 monolayer [Hoffman, A. N. et al.. *npj 2D Mater. Appl.* **2019**, 3(1), 50.], in this work, we use density functional theory (DFT) to further explore the thermal, dynamic, and mechanical stability of monolayer PdO_2 and study its structural and electronic properties. We further studied its vertical heterojunction composed of 1T-PdO_2 and graphene monolayers. We show that both the monolayer and the heterojunction are energetically and dynamically stable with no negative frequencies in the phonon spectrum and belong to the vdW-type. 1T-PdO_2 is an indirect-band-gap semiconductor with band-gap values of 0.5 eV (GGA) and 1.54 eV (HSE06). The interface properties of the heterojunction show that the n-type Schottky barrier height (SBH) becomes negative at the vertical interface in the PdO_2/graphene contact, forming an Ohmic contact and mainly suggesting the potential of graphene for efficient electrical contact with the PdO_2 monolayer. However, at the same time, a negative band bending occurs at the lateral interface based on the current-in-plane model. Moreover, the optical absorption of the PdO_2/graphene heterojunction under visible-light irradiation is significantly enhanced compared to the situation in their free-standing monolayers.

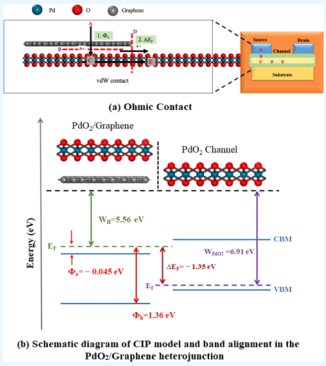

1. INTRODUCTION

Transition-metal dichalcogenides (TMDs) have captured the attention of researchers due to their remarkable properties and their potential applications in electronic devices,[1−3] optoelectronics,[4,5] valleytronics,[6,7] light-emitting diodes (LEDs),[8] solar cells,[9] field-effect transistors (FETs),[10] optical-light eliminators,[11] modulators,[12] laser accessories,[13] and catalysis.[14] Generally, TMDC monolayers exhibit two common polymorphs, namely, trigonal prismatic (H-phase) and octahedral coordinated (T-phase).[15−17] The H-phase belongs to the D_{3h} point group having the $P\bar{6}m2$ space group, and the T-phase belongs to the D_{3d} point group having the $P\bar{3}m$ 1 space group.[15,18] Both experimentally and theoretically, it has been found that the arrangement of chalcogenide atoms significantly alters the properties of those monolayers.[19,20] Very recently, Hoffman et al., while studying the air stability of monolayer $PdSe_2$, reported the formation of PdO_2 on the surface due to the chemisorption of the O_2 molecule, where oxygen atoms replace the Se atoms.[21] Monolayer PdO_2 refers to a single layer of palladium oxide (PdO_2) atoms arranged in a two-dimensional (2D) structure. Palladium oxide is a compound composed of palladium and oxygen and is a well-known catalyst used in various chemical reactions. The unique properties of monolayer PdO_2 make it an attractive material for use in catalysis, electronics, and other applications.[22,23] Researchers are actively studying the properties and potential applications of monolayer PdO_2, including in electrocatalysis, hydrogen storage, and sensing.[22,23] The development of monolayer PdO_2 has opened up new possibilities for the design of advanced materials with unique properties and improved performance.

Graphene, a two-dimensional (2D) material composed of a single layer of carbon atoms, has attracted significant attention due to its exceptional electrical, mechanical, and thermal properties.[24] However, its zero band gap and high electrical conductivity limit its applications in electronic devices such as field-effect transistors (FETs). To overcome this challenge, the band-gap opening in graphene has been a subject of intense research.[25−27] One approach is to form a van der Waals (vdW) heterojunction with another 2D material, such as transition-metal oxides, to open a band gap in graphene. The rapid advancements in two-dimensional (2D) materials and their heterostructures have led to the emergence of truly 2D physics with unique phenomena. These developments have also given rise to innovative heterostructure devices like tunneling transistors and light-emitting diodes. Therefore, innovation of new 2D vdW heterojunctions based on novel 2D materials is scientifically desirable to develop environment-friendly and energy-efficient optoelectronic applications.[18,28−31]

Received: February 9, 2024
Revised: June 8, 2024
Accepted: June 11, 2024
Published: June 20, 2024

Here, we report on the stability as well as electronic and mechanical properties of monolayer PdO_2. We show that the monolayer is energetically stable in the 1T phase rather than in the 2H phase. Furthermore, the phonon dispersion mode for the monolayer confirms the dynamic stability. The energy band gap lies within the semiconducting range and can be further tuned for nanoelectronic applications. The energy band-gap calculations show a band-gap opening in graphene by forming a vdW heterojunction with the 2D-PdO_2 layer. Our results showed that the graphene-PdO_2 vdW heterojunction exhibited an n-type Ohmic contact with a low resistance of about 1 kΩ. Furthermore, we found that the band-gap opening in graphene is induced by the formation of a vdW heterojunction with the monolayer PdO_2. The band-gap opening is confirmed by the observed shift in the Dirac point in the graphene's density of states. The magnitude of the band-gap opening is found to be proportional to the thickness of the PdO_2 sheet, which confirms the effectiveness of the vdW heterojunction in opening a band gap in graphene.

2. COMPUTATIONAL METHODS

All of our calculations are performed using the density functional theory (DFT) implemented in the Vienna ab initio simulation package (VASP).[32] The generalized gradient approximation (GGA) with the parametrization scheme of Pardew−Burke−Ernzerhof (PBE) is applied for the electron exchange correlation processes, whereas the electron−ion interactions are processed by the projector augmented wave (PAW) method.[33] However, the Heyd−Scuseria−Ernzerhof (HSE06) hybrid functional,[34,35] which includes the Hartree−Fock exchange energy and the Coulomb screening effect, is used to calculate the electronic and optical properties.[36] A cutoff energy of 500 eV is chosen for the plane-wave expansion of the electronic Eigen functions for the monolayer PdO_2. The force criterion for the atomic relaxation is chosen as 0.001 eV/Å. The periodic images of monolayers of PdO_2 are separated by a distance of 20 Å so as to bypass the interlayer interactions. K-point sampling with a $6 \times 6 \times 1$ mesh is used for the integration of the Brillouin zone (BZ). The finite difference method is used to calculate the elastic constants.[37] The displacement step size is selected as 0.015 Å using displacement for each ion in the x and y directions. Phonon calculations are performed using the finite displacement method as implemented in the Phonopy program.[38] A dipole correction is added to compensate for the dipole interactions.[39] In addition, the van der Waals density functional of optB886-vdW is considered for all of the calculations to describe the effect of vdW interactions.[40,41] A $5 \times 5 \times 1$ supercell is considered for *ab initio* molecular dynamics (AIMD) simulations at 300 K with each time step of 1 fs to test the thermal stability of the monolayer PdO_2 at room temperature.[42−44] All optical properties can be deduced from the complex dielectric function (ε)

$$\varepsilon(\omega) = \varepsilon_1(\omega) + i\varepsilon_2(\omega) \tag{1}$$

The real ($\varepsilon_1(\omega)$) and imaginary (Img.) ($\varepsilon_2(\omega)$) parts of the dielectric function are associated with electronic polarization and absorption of the crystal structure. The imaginary part of the complex dielectric function can be evaluated by momentum matrix relations between occupied and unoccupied wave functions, and $\varepsilon_1(\omega)$ can be calculated from $\varepsilon_2(\omega)$ by using Kramer−Kronig expressions[45]

$$\varepsilon_2(\omega) = \frac{2e^2\pi}{\Omega\epsilon_0} \sum_{k,v,c} |\langle \psi_k^c | \hat{u} \times r | \psi_k^v \rangle|^2 \, \delta(E_k^c - E_k^v - E) \tag{2}$$

$$\varepsilon_1(\omega) = 1 + \left(\frac{2}{\pi}\right) \int_0^\infty d\omega' \frac{\omega'^2 \varepsilon_2(\omega')}{\omega'^2 - \omega^2} \tag{3}$$

In the above equations, $\hat{u}$, e, ψ_k^c, and ψ_k^v denote the vectors that describe the polarization of the incident electric field, electronic charge, and the wave functions of the conduction band (CB) and the valence band (VB), respectively. Therefore, all other optical constants including the absorption coefficient $a(\omega)$, reflectivity $R(\omega)$, energy loss function $L(\omega)$, and the real part of optical conductivity $\sigma(\omega)$ can be evaluated by the function of $\varepsilon(\omega)$ using the following formulas

$$a(\omega) = \sqrt{2}\,\omega \left[\sqrt{\varepsilon_1^2(\omega) + \varepsilon_2^2(\omega)} - \varepsilon_1(\omega) \right]^2 \tag{4}$$

$$R(\omega) = \left| \frac{\sqrt{\varepsilon_1(\omega) + j\varepsilon_2(\omega)} - 1}{\sqrt{\varepsilon_1(\omega) + j\varepsilon_2(\omega)} + 1} \right|^2 \tag{5}$$

$$L(\omega) = \mathrm{Im}\left(\frac{-1}{\varepsilon(\omega)}\right) = \frac{\varepsilon_2(\omega)}{\varepsilon_1^2(\omega) + \varepsilon_2^2(\omega)} \tag{6}$$

$$Re[\sigma(\omega)] = \frac{\omega}{4\pi}\varepsilon_2(\omega) \tag{7}$$

3. RESULTS AND DISCUSSION

3.1. Structural and Electronic Properties of PdO_2. The top and side views of the 1T phase of monolayer PdO_2 are shown in Figure 1. Most of the results have been calculated using the ABC structure of the PdO_2 monolayer. The atomic position

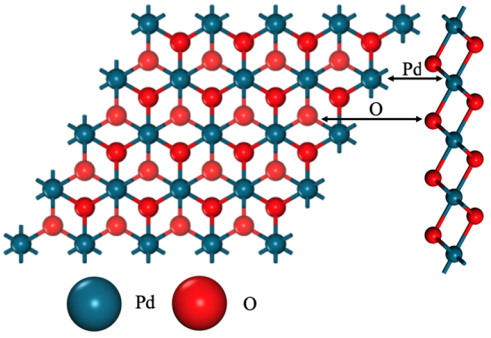

Figure 1. Top and side views of a portion of the 1T phase of the monolayer PdO_2; the teal, red-colored solids spheres represent the Pd and O atoms, respectively.

Table 1. Comparison between Different Parameters of the 1T and 2H-PdO_2 Monolayers[a]

	ML PdO_2	
	1T	2H
$a = b$ (Å)	3.101 A	3.048 A
E_0 (eV)	−16.0723	−13.726
E_f (eV)	−11.5384	−9.1925
Pd−O (Å)	2.044	2.136

[a]Here, a and b represent the calculated lattice parameters, E_0 and E_f represent the total energy and formation energy, and Pd−O represents the bond length of the monolayer PdO_2.

https://doi.org/10.1021/acsomega.4c01305
ACS Omega 2024, 9, 28176−28185

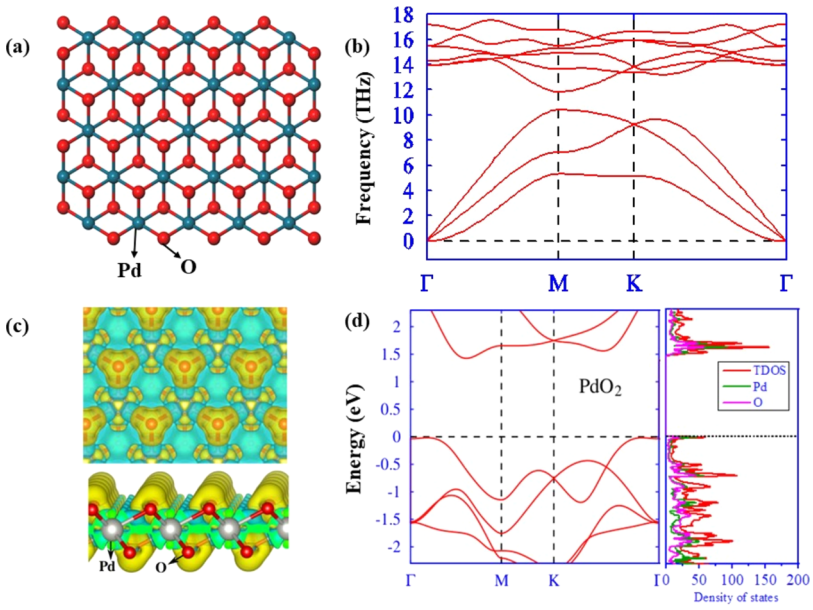

Figure 2. (a) Thermodynamic stability, (b) phonon dispersion modes, (c) top and side views of charge density difference (the yellow color indicates electron gain, while the light-blue color shows electron loss at the isosurface of 5×10^{-3} e/Å^3, and (d) band structure and projected density of states for the 1T phase of ML PdO_2.

Table 2. Comparison between In-Plane Young's Moduli (Y), Poisson's Ratio (ν), and Elastic Moduli (C_{11} and C_{12}) for Monolayers of Graphene, MoS_2, and PdO_2

monolayers	Y (N m^{-1})	ν	C_{11} (N m^{-1})	C_{12} (N m^{-1})
graphene[55]	340.8	0.178	352.0	62.6
MoS_2 monolayer[56]	120.1	0.254	128.4	32.6
PdO_2	108.116	0.234	114.3855	26.78

and lattice vectors are optimized in order to study the strain effects on the electronic structure of the PdO_2 monolayer. The optimized lattice parameters and bond lengths of the monolayer with 1T and 2H phases are listed in Table 1.

The formation energy per atom (E_f) for the monolayer PdO_2 is defined by the relation $E_f = E_{PdO_2} - E_{Pd} - 2E_O$, where E_{PdO_2} is the total energy of the unit cell of a monolayer PdO_2 and E_{Pd} and E_O are the energies of an isolated atom of Pd and O, respectively. According to this equation, the E_f energies for monolayers are −11.54 and −9.19 eV/atom for 1T and 2H phases, respectively. These results reveal that thermodynamically the 1T phase of monolayer PdS_2 is more favorable than it 2H-phase, as shown in Figure 2a.

To evaluate the dynamic stability, we calculated the phonon dispersion of the monolayer PdO_2, as shown in Figure 2b. There are no imaginary modes in the entire Brillouin zone, depicting that monolayer PdO_2 is dynamically stable. Three acoustic modes and six optical modes are found in the phonon dispersions. The acoustic modes include a transverse acoustic mode, a longitudinal acoustic mode, and a flexural acoustic mode. The flexural mode has a quadratic shape near the Γ-point, while the TA and LA modes are linear. This behavior of the acoustic modes is well-matched with other previously reported monolayers such as MoS_2, WS_2, W_2C, and SnS_2.[46−50] Further, to determine the mechanical stability of monolayer PdO_2, the finite displacement method is used. To calculate its elastic tensor, the elastic constants C_{11} are noticed to be equal to C_{22}, whereas $C_{12} = C_{21}$ due to the hexagonal symmetry. The mechanical stability of these monolayers is guaranteed by Born stability criteria, i.e., $C_{11} + C_{22} - 2C_{12} > 0$ and C_{11}, C_{66}, and $C_{22} > 0$.[51] The in-plane Young's modulus (Y) is defined as $Y = (C_{11}^2 - C_{12}^2)/C_{11}$. The Y value thus calculated for PdO_2 (108.116 N/m) is well comparable to other monolayers like SnS_2 and phosphorene.[52,53] The Poisson's ratio (ν) is defined as $\nu = C_{12}/C_{11}$, and the calculated value is 0.234. The lower value of Young's modulus for PdO_2 compared to PdS_2 (116.4 N/m) and $PtSe_2$ (115.9 N/m) comes from the fact that they have different structures. While Pd is 4-fold coordinated in the $PdS_2/PdSe_2$ structures, it is 6-fold coordinated in the PdO_2 structure. The elastic moduli results are summarized in Table 2, where a comparison with other well-known 2D materials is also presented. The charge density difference ($\Delta\rho$) is defined by $\Delta\rho = \rho_{PdO_2} - \rho_{Pd} - \rho_{O_2}$ (in units of e/Å^3). These bonding charge distributions clearly show the electron accumulation in O and depletion in Pd, and the amount of charge localized in this region qualitatively indicates the strength of the PdO_2 bond; see Figure 2c. The band structure along high symmetry points and density of states for the PdO_2 monolayer are shown in Figure 2d. It is evident from Figure 2d that the monolayer of PdO_2 has an indirect band gap. Our calculations result in band gaps of 0.50 and 1.54 eV with the GGA and HSE06 functionals. The HSE06 functional is more accurate. Although it provides qualitatively similar descriptions of band structures of these materials, due to addition of direct exchange, the band gaps increased considerably. The band gap for the PdS_2 monolayer using the HSE06 functional is reported as 1.6 eV, which is higher than PdO_2.[54] Usually, the decreasing band-gap trend is found in TMD down the group of chalcogen atoms. However, here, PdO_2 and $PdS_2/PdSe_2$ have completely different geometries. In PdO_2, the Pd atom is 6-fold coordinated with the O atom, whereas in $PdS_2/PdSe_2$, it is 4-fold coordinated. PDOS analysis (Figure 2d) reveals the nature of the bonding in these materials. In general, the valence band is dominated by hybridization between Pd and O's p states, while the conduction band is mostly populated by the states of O atoms.

https://doi.org/10.1021/acsomega.4c01305
ACS Omega 2024, 9, 28176−28185

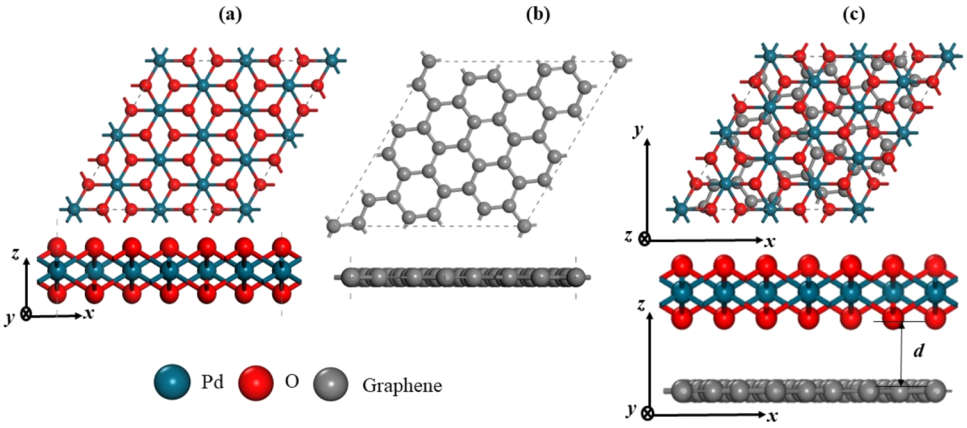

Figure 3. (a) Top and side views of a $2\times \sqrt{3}$ supercell of free-standing PdO_2 monolayer. (b) Top and side views of a $2\times \sqrt{2}$ supercell of graphene. (c) Schematic diagram with side and top views of the PdO_2/graphene heterojunction. Teal, red, and gray spheres indicate palladium, oxygen, and graphene atoms, respectively.

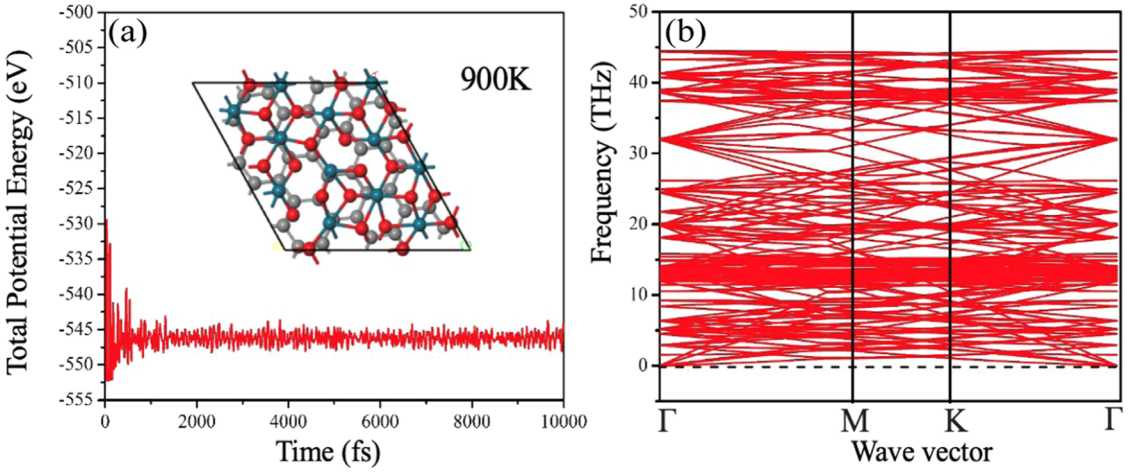

Figure 4. (a) Total potential energy fluctuation at 900 K up to 1 fs using AIMD simulation. (b) Phonon spectrum of the PdO_2/graphene heterojunction.

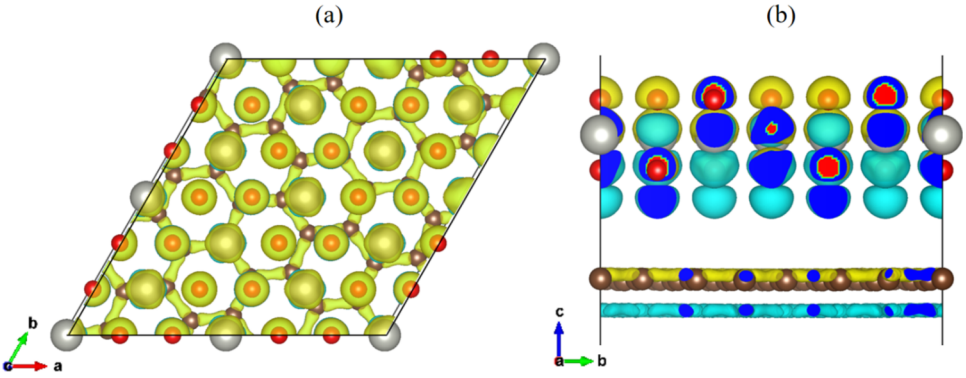

Figure 5. (a) Top and (b) side views of the 3D plot of the charge density difference, where yellow and blue regions show charge accumulation and charge depletion.

4. PDO_2/GRAPHENE HETEROJUNCTION

4.1. Geometry and Stability. A heterostructure of monolayer PdO_2 with metallic graphene is designed to study its electronic properties. We construct the PdO_2/graphene heterojunction by vertically stacking the two monolayers. Monolayer PdO_2 and graphene both have a hexagonal geometry, but they differ in lattice constants, which leads to unacceptable lattice mismatch. To reduce this lattice mismatch to an acceptable value, we combine a $2 \times \sqrt{3}$ supercell of monolayer PdO_2 with a $2 \times \sqrt{2}$ supercell of graphene, as illustrated in Figure 3. Thus, the lattice mismatch is reduced to less than 1% with the least possible number of Pd, O, and C atoms. The relaxed configuration is shown in Figure 3c. We note that after optimization, both the PdO_2 and graphene layers remain intact without any obvious geometric changes, implying that the lattice strain is negligible in this heterojunction. To examine the

https://doi.org/10.1021/acsomega.4c01305
ACS Omega 2024, 9, 28176−28185

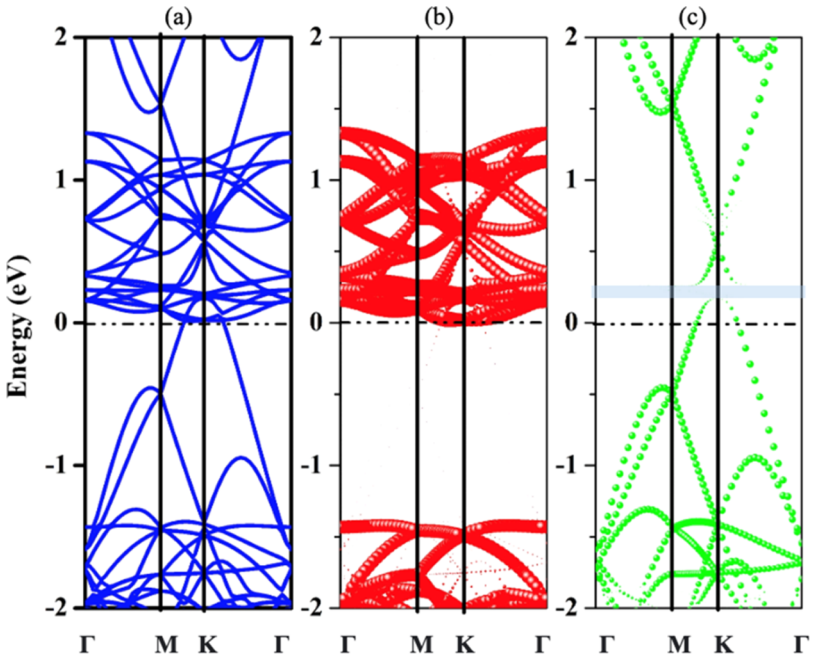

Figure 6. (a) Total band structure, (b) projected band structure of PdO_2 (red bands), and (c) projected band structure of graphene (green bands). The Fermi level was shifted to zero energy.

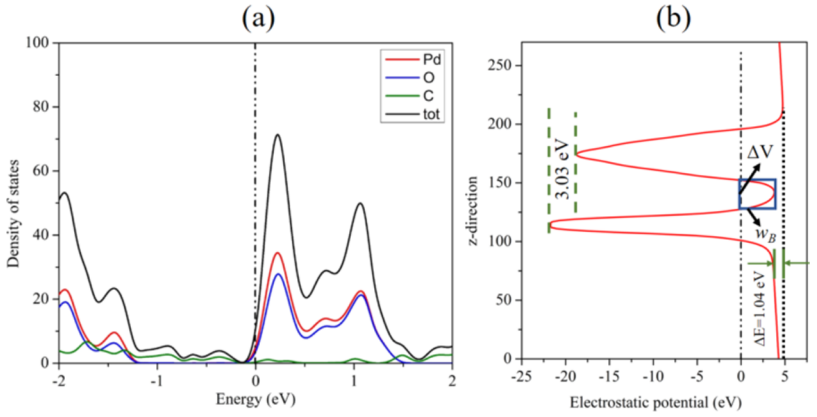

Figure 7. (a) Projected density of states (PDOS) and (b) electrostatic potential profile of the PdO_2/graphene heterojunction. The Fermi level was shifted to zero energy.

stability of PdO_2/graphene, we calculated its binding energy E_b, defined by $E_b = (E_{PdO2/G} - E_{PdO2} - E_G)/A$, where $E_{PdO2/G}$ is the total energy of the PdO_2/graphene heterojunction, E_{PdO2} is the total energy of the individual monolayer PdO_2, E_G is the total energy of graphene, and A is the area of the heterojunction. The calculated binding energy (E_b) is ∼ −480 meV/Å^2. The obtained E_b has a comparable magnitude as that of other vdW heterojunctions such as pentagraphene/graphene,[57] SnSe/graphene,[58,59] graphene/phosphorene,[60] and GeSe/SnSe[61,62] heterojunctions, implying that the PdO_2/graphene heterojunction can be classified as a vdW heterojunction.

To further validate the stability of the PdO_2/graphene heterojunction, we applied ab initio molecular dynamics (AIMD) simulations using a canonical (NVT) ensemble to study the thermal stability of the PdO_2/graphene heterojunction and phonon calculation to find the phonon stability; see Figure 4a. We first perform the simulation at 300 K for 10 ps with a time step of 1 fs and increase the temperature to 600 K and then to 900 K. The fluctuations of the total energy with simulation time at 900 K are plotted in Figure 4a. After 10,000 steps, no permanent distortions in geometry or the total energy were observed, which confirms its thermal stability. As shown in Figure 4b, the phonon dispersion curves along the entire Brillouin zone (Γ-M-K-Γ) of the PdO_2/graphene heterojunction have no imaginary frequency mode, indicating its dynamic stability. To investigate the interlayer coupling between the PdO_2 monolayer and graphene, we also calculated the differential charge density between them [see Figure 5]. The xy-plane-averaged differential charge density is defined according to the equation $\Delta\rho(z) = \rho_{PdO2/graphene}(z) - \rho_{graphene}(z) - \rho_{PdO2}(z)$, where $\rho_{PdO2/graphene}(z)$, $\rho_{graphene}(z)$, and $\rho_{PdO2}(z)$ represent the averaged plane charge densities of the PdO_2/graphene heterojunction, graphene, and free-standing PdO_2 monolayers, respectively. The top and side views of the three-dimensional (3D) charge density plot are given in Figure 5, which shows the charge density redistribution in the form of electron-rich and hole-rich regions in the heterojunction.

https://doi.org/10.1021/acsomega.4c01305
ACS Omega 2024, 9, 28176−28185

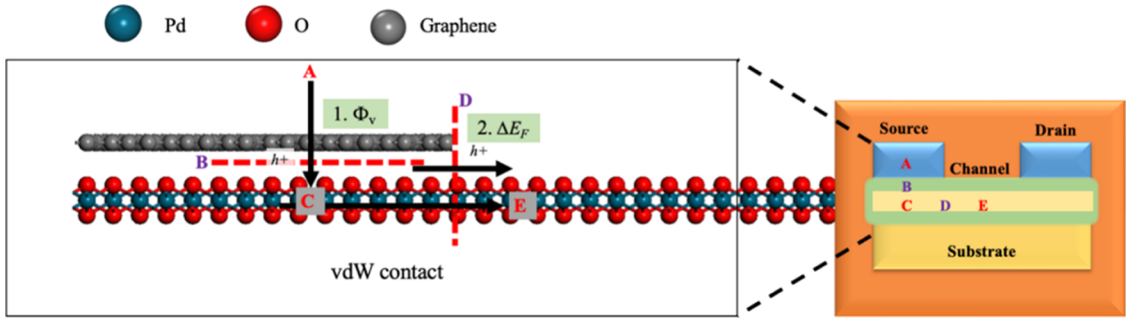

Figure 8. On the left side: a typical illustration of the PdO_2/graphene heterojunction. A, C, and E represent the three regions, whereas B and D are the two distinguished interfaces. The black arrows show the pathway of an electron or hole moving from the metal electrode to the PdO_2 channel (A to B to C to D to E). Φv is the Schottky barrier, and ΔE_F is the band bending. The inset on the right side shows the schematic of a typical field-effect transistor (FET), with source and drain contacts, and the channel region.

5. ELECTRONIC PROPERTIES

To clearly understand the electronic properties of the stacked system, the band structure is calculated as shown in Figure 6a, and the band structures of ML PdO_2 and graphene are well-preserved upon forming the heterojunction, consistent with the important feature of vdW contacts. From Figure 6b,c, we obtain two results: (i) the Fermi level has moved into the conduction band of the heterojunction, leading to an n-type Ohmic contact; and (ii) a band-gap opening in graphene at the Dirac point of ∼0.10 eV can be observed, which is because the TMDs introduce an asymmetry in the crystal lattice structure, leading to a breaking of the inversion symmetry in the combined material as reported on combination with MoS_2, WS_2, PdS_2, etc. This band-gap opening is significant because it allows the combined material to exhibit a semiconductor-like behavior, which is essential for developing electronic devices such as transistors and sensors. The size of the band gap can be controlled by varying the thickness of the TMD layer, which can lead to the development of devices with tunable electronic properties as reported in other studies.[58] To further study the band offset nature of the PdO_2/graphene heterostructure, the total density of states (TDOS) and the orbital resolved projected density of states (PDOS) are also studied as shown in Figure 7a.[63,64] As shown, the valence band maximum (VBM) has contribution made by both graphene and PdO_2 electrons, and there is no density of states between −1.18 and −0.10 eV of PdO_2 maintaining its band gap, which agrees well with the electronic band structure, and the Fermi level has also moved into the conduction band. The conduction band maximum (CBM) as shown is, however, mostly dominated by the electrons of PdO_2.

The electrostatic potential profiles (Figure 7b) of the PdO_2/graphene heterojunction along the z direction reveal the existence of a tunneling barrier between the stacked systems. From Figure 7b, we can see that there is a large potential drop of 3.02 eV at the interface of the PdO_2/graphene heterojunction, implying that electrons are transferred from graphene to PdO_2 and form an internal electric field at the interface. This large potential drop shows that there will be a low rate of electron−hole pair recombination, making it a potential candidate for photoelectric device applications. We also evaluate the tunneling possibility (T_P) of the PdO_2/graphene heterojunction based on the Wetzel−Kramer−Brillouin (WKB) approximation[65]

$$T_P = \exp\left(-2\frac{\sqrt{2m\Delta V}}{\hbar} \times w_B \right) \quad (8)$$

where ΔV and w_B represent, respectively, the height and width of the tunneling barrier potential, m denotes the effective mass of the free electron, and $\hbar$ is the approximate Planck's constant. From the electrostatic potential profile (marked by the blue rectangle in Figure 7b), the calculated ΔV and w_B are 3.97 Å and 23.4 eV, respectively, which lead to a T_P of 79.5% in the PdO_2/graphene heterojunction. Compared to $PdSe_2$/Pb (9.18%) and $PdSe_2$/Au (18%),[66] the relatively high T_P of the PdO_2/graphene heterojunction enables efficient charge transport across the heterojunction for high-performance FET devices.

6. EXTENDED APPLICATION

To enable the movement of charge carriers from the electrode to the channel material in a device, two types of barriers must be overcome: (i) the Schottky barrier (Φ_{SB}), which governs the charge transfer between the metal and the semiconductor at the vertical interface; and (ii) the band bending ΔE_F, which occurs at the lateral interface between the electrode and the channel

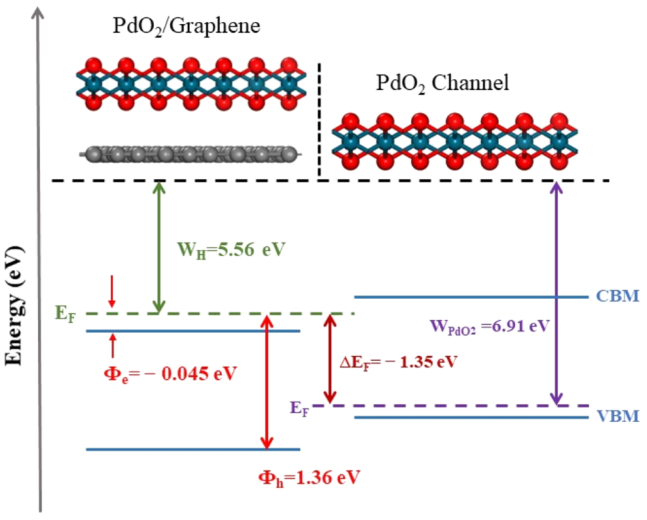

Figure 9. Schematic diagram of the CIP model and band alignment in the PdO_2/graphene heterojunction, where W_H and W_{PdO2} are the work functions of the PdO_2/graphene heterojunction and the noncontacted PdO_2 monolayer, and E_F is the Fermi-level energy. The black, green, and purple dashed lines show the interface between the PdO_2/graphene heterojunction and the noncontacted PdO_2 channel, E_{vac}, and E_F, respectively. The blue solid lines indicate the CBM and VBM regions of the PdO_2/graphene heterojunction and the noncontacted PdO_2 channel.

https://doi.org/10.1021/acsomega.4c01305
ACS Omega 2024, 9, 28176−28185

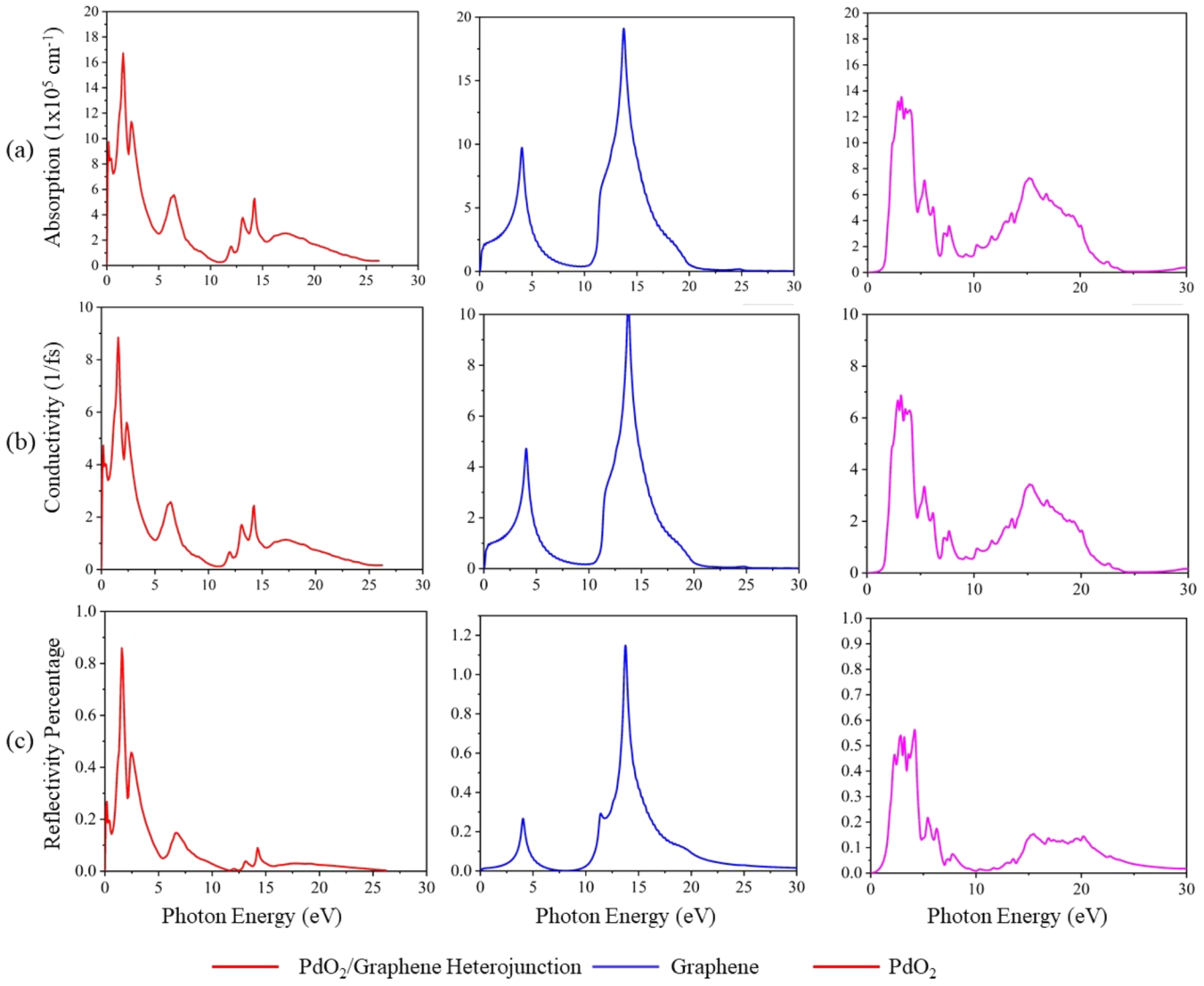

Figure 10. (a) Absorption coefficient, (b) optical conductivity, and (c) reflectivity percentage for the graphene/PdO_2 heterojunction and graphene and PdO_2 monolayers.

interface. A typical illustration of the PdO_2/graphene heterojunction for the FET device is shown in Figure 8, where the PdO_2/graphene heterojunction acts as an electrode and the free-standing PdO_2 monolayer as a channel region. The Schottky barrier between the two materials is the most critical parameter in determining the contact resistance. The Schottky barrier height (SBH) can be calculated using the Schottky−Mott rule,[59] which defines it as the energy difference between the Fermi level (E_F)[67] of the heterojunction and the energy band edges of the semiconductor, namely, the conduction band minimum (CBM) and the valence band maximum (VBM), identified from the projected electronic band structure [Figure 6b].[60,68,69]

$$\Phi_{SB-n} = E_{CBM} - E_F,\ \Phi_{SB-P} = E_F - E_{VBM} \quad (9)$$

where Φ_{SB-n} and Φ_{SB-P} are the n-type and p-type SBHs, respectively.

To minimize contact resistance in device applications, a low Schottky barrier height (Φ_{SB}-e or Φ_{SB}-h) is desirable. Following the Schottky−Mott rule,[59] a Schottky-barrier-free contact is achievable when the Schottky barrier height becomes zero or negative, allowing for spontaneous carrier infusion from the stacked system to the PdO_2 channel. In the PdO_2/graphene contact, the Φ_{SB}-n is −45 meV and the Φ_{SB}-p is 1.36 eV, indicating the formation of an Ohmic contact and demonstrating graphene's potential as an efficient electrical contact with (ML) PdO_2 with high charge carrier efficiency.

The band alignment of the PdO_2/graphene contact is also important in designing new materials and devices and can be estimated by using the vacuum level as the common energy reference. A current-in-plane (CIP) model is used to estimate the band bending in the PdO_2/graphene contact. The band bending is determined by the Fermi-level difference denoted as ΔE_F; at the lateral interface, "D" is estimated as $\Delta E_F = W_H - W_{PdO2} = -1.35$ eV, indicating that electrons are the major carriers making the channel n-type, similar to the case of the MoS_2/graphene-based device. Figure 9 shows the PdO_2/graphene heterojunction on the left and the free-standing PdO_2 sheet on the right.[68,69]

7. OPTICAL PROPERTIES

The optical response of the 1T-PdO_2/graphene vdW heterostructures tends to improve due to the interfacial interactions between its layers. This improvement in optical response has a considerable effect on the optoelectronic device's performance,

https://doi.org/10.1021/acsomega.4c01305
ACS Omega 2024, 9, 28176−28185

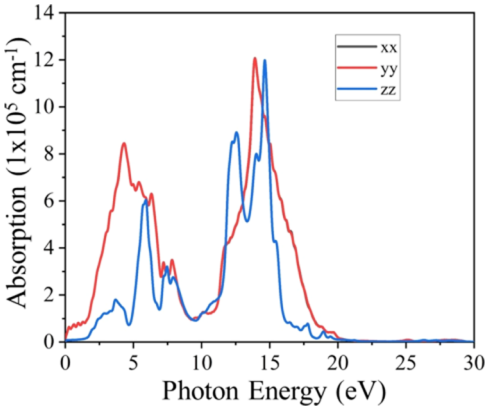

Figure 11. Absorption coefficient of the PdO_2/graphene heterojunction.

such as solar cells and photodetectors, as it enhances their efficiency and sensitivity to light. In this study, we determine both the real and imaginary components of the dielectric function for 1T-PdO_2/graphene vdW heterostructures. Using the concept of optical properties, we derive the absorption coefficient, optical conductivity, and reflectivity percentage. The optical absorption coefficient is a measure of how strongly a material absorbs light of a particular frequency or wavelength, denoted by ω. In Figure 10a, we observe several strong absorption peaks at 0.18, 0.4, 1.56, and 2.36 eV, hence providing many channels for dipole transitions. This is due to internal photon scattering within the atomic particles. As for optical conductivity, the PdO_2/graphene heterojunction exhibits a substantial conduction in the visible region and the near-ultraviolet region (see Figure 10b). In particular, we find several peaks at 0.25, 1.59, 2.28, and 6.09 eV that are missing from both graphene and monolayer PdO_2 with corresponding optical conductivities of 4.78×10^5, 8.89×10^5, 5.62×10^5, and 2.57×10^5 cm^{-1}, respectively. The reflectivity percentage of the PdO_2/graphene heterojunction as shown in Figure 10c is increased significantly compared with those of the free-standing PdO_2 and graphene. The maximum reflection of the PdO_2/graphene heterojunction is observed around 29% in the visible region, which rapidly drops to 18% from 0 to 0.60 eV. It again starts to increase toward higher energy ranges, and a maximum reflection of around 84% is observed between energy ranges from 2.5 to 5 eV in the UV region. It is worth mentioning that the electron−hole interaction is not considered while calculating the optical properties of PdO_2, graphene, and PdO_2/graphene heterojunction in this study. The GW approximation combined with the Bethe−Salpeter equation (GW + BSE) can accurately describe the optical response by introducing self-energy corrections and capturing excitonic effects.[70] However, it is computationally too expensive for this system due to its large size. We use the Kubo−Greenwood method to calculate the dielectric tensor, where the imaginary part is the sum of occupied and unoccupied bands of the dipole matrix elements.[71] Our calculated results can provide a qualitative understanding of the optical behavior of this system. It is obtained from the optical characterization that these heterostructures show anisotropic optical behavior [see Figure 11]. This anisotropic optical property is very important in photonic devices, specifically in photodetectors.

8. CONCLUSIONS

In conclusion, our results show that 2D 1T-PdO_2 is both energetically and dynamically stable with semiconducting electronic properties, and the formation of a vdW heterojunction between graphene and 2D 1T-PdO_2 sheets results in an n-type Ohmic contact and enhanced optical performance. This work opens up new opportunities for the development of graphene-based electronic devices, such as FETs and photodetectors, which require a band gap and low resistance for efficient device operation. Furthermore, the vdW heterojunction approach offers a scalable and cost-effective method for the large-scale production of graphene-based electronic devices as it does not require high-temperature processing or complicated patterning techniques.

AUTHOR INFORMATION

Corresponding Authors

Muhammad Yar Khan − *Foundation department Qilu Institute of Technology, Jinan 250200 Shandong, P. R. China; School of Materials Science and Engineering, Zhejiang University, Hangzhou 310027, P. R. China;* orcid.org/0000-0002-7376-6790; Email: hmyarkhan@yahoo.com

Arzoo Hassan − *College of Physics and Optoelectronic Engineering, Shenzhen University, Guangdong 518060, P. R. China*; Email: arzoo.hassan11@hotmail.com

Authors

Abdus Samad − *Department of Physics, University of Ulsan, Ulsan 44610, Republic of Korea*

Abdullah Al Souwaileh − *Department of Chemistry, College of Science, King Saud University, Riyadh 11451, Saudi Arabia*

Complete contact information is available at: https://pubs.acs.org/10.1021/acsomega.4c01305

Notes

The authors declare no competing financial interest.

ACKNOWLEDGMENTS

This project was supported by the Researchers Supporting Project (number RSP2024R238), King Saud University, Riyadh, Saudi Arabia. This work was also supported by the Guangdong Basic and Applied Basic Research Foundation (2021A1515010082) and the Shenzhen Fundamental Research Program (JCYJ20190808121405740).

REFERENCES

(1) Radisavljevic, B.; Radenovic, A.; Brivio, J.; Giacometti, V.; Kis, A. Single-layer MoS_2 transistors. *Nat. Nanotechnol.* **2011**, *6* (3), 147−150.

(2) Akinwande, D.; Petrone, N.; Hone, J. Two-dimensional flexible nanoelectronics. *Nat. Commun.* **2014**, *5* (1), No. 5678.

(3) Wang, H.; Yu, L.; Lee, Y. H.; Shi, Y.; Hsu, A.; Chin, M. L.; Li, L. J.; Dubey, M.; Kong, J.; Palacios, T. Integrated circuits based on bilayer MoS_2 transistors. *Nano Lett.* **2012**, *12* (9), 4674−4680.

(4) Yin, Z.; Li, H.; Li, H.; Jiang, L.; Shi, Y.; Sun, Y.; Lu, G.; Zhang, Q.; Chen, X.; Zhang, H. Single-layer MoS_2 phototransistors. *ACS Nano* **2012**, *6* (1), 74−80.

(5) Lopez-Sanchez, O.; Lembke, D.; Kayci, M.; Radenovic, A.; Kis, A. Ultrasensitive photodetectors based on monolayer MoS_2. *Nat. Nanotechnol.* **2013**, *8* (7), 497−501.

(6) Luo, Y.; McDowell, L.; Su, L.; Liu, Y.; Qiu, J.; Shi, Z. Enhanced performance in uncooled n-CdSe/p-PbSe photovoltaic detectors by high-temperature chloride passivation. *RSC Adv.* **2022**, *12* (14), 8423−8428.

(7) Mak, K. F.; He, K.; Shan, J.; Heinz, T. F. Control of valley polarization in monolayer MoS_2 by optical helicity. *Nat. Nanotechnol.* **2012**, *7* (8), 494−498.
(8) Song, J.; Kim, K. H.; Kim, E.; Moon, C. K.; Kim, Y. H.; Kim, J. J.; Yoo, S. Lensfree OLEDs with over 50% external quantum efficiency via external scattering and horizontally oriented emitters. *Nat. Commun.* **2018**, *9* (1), No. 3207.
(9) Bora, S. R.; Kalita, D. J. Hopping transport in perylene diimide based organic solar cells: a DFT approach. *New J. Chem.* **2022**, *46* (40), 19357−19372.
(10) Kim, H. P.; Vasilopoulou, M.; Ullah, H.; Bibi, S.; Gavim, A. E. X.; Macedo, A. G.; da Silva, W. J.; Schneider, F. K.; Tahir, A. A.; Teridi, M. A. M.; Gao, P.; Yusoff, A.; Nazeeruddin, M. K. A hysteresis-free perovskite transistor with exceptional stability through molecular cross-linking and amine-based surface passivation. *Nano Scale* **2020**, *12* (14), 7641−7650.
(11) Tedjeuguim, C. T.; Tasheh, S. N.; Alongamo, C. I. L.; Ghogomu, J. N. A DFT and TD-DFT study of charge transport and non-linear optical properties of N-(4- methoxybenzylidene)isonicotinohydrazone, 2,2′-bipyridine and their Fe_2+, Ni_2+, Cu_2+, Pd_2+ and Pt_2+ complexes. *J. Chem. Sci.* **2022**, *134* (3), No. 70.
(12) Husain, M.; Rahman, N.; Albalawi, H.; Ezzine, S.; Amami, M.; Zaman, T.; Rehman, A. U.; Sohail, M.; Khan, R.; Khan, A. A.; Tahir; Khan, A. Examining computationally the structural, elastic, optical, and electronic properties of $CaQCl_3$ (Q = Li and K) chloroperovskites using DFT framework. *RSC Adv.* **2022**, *12* (50), 32338−32349.
(13) Wang, P.; Fang, F. Real-time time-dependent DFT study of laser-enhanced atomic layer etching of silicon for damage-free nanostructure fabrication. *J. Appl. Phys.* **2022**, *132* (14), No. 144303.
(14) Voiry, D.; Yang, J.; Chhowalla, M. Recent Strategies for Improving the Catalytic Activity of 2D TMD Nanosheets Toward the Hydrogen Evolution Reaction. *Adv. Mater.* **2016**, *28* (29), 6197−6206.
(15) Kan, M.; Wang, B.; Lee, Y. H.; Sun, Q. A density functional theory study of the tunable structure, magnetism and metal-insulator phase transition in VS_2 monolayers induced by in-plane biaxial strain. *Nano Res.* **2015**, *8* (4), 1348−1356.
(16) Qorbani, M.; Sabbah, A.; Lai, Y. R.; Kholimatussadiah, S.; Quadir, S.; Huang, C. Y.; Shown, I.; Huang, Y. F.; Hayashi, M.; Chen, K. H.; Chen, L. C. Atomistic insights into highly active reconstructed edges of monolayer 2H-WSe_2 photocatalyst. *Nat. Commun.* **2022**, *13* (1), No. 1256.
(17) Tang, S.; Zhang, C.; Wong, D.; Pedramrazi, Z.; Tsai, H.-Z.; Jia, C.; Moritz, B.; Claassen, M.; Ryu, H.; Kahn, S.; Jiang, J.; Yan, H.; Hashimoto, M.; Lu, D.; Moore, R. G.; Hwang, C.-C.; Hwang, C.; Hussain, Z.; Chen, Y.; Ugeda, M. M.; Liu, Z.; Xie, X.; Devereaux, T. P.; Crommie, M. F.; Mo, S.-K.; Shen, Z.-X. Quantum spin Hall state in monolayer 1T′-WTe_2. *Nat. Phys.* **2017**, *13* (7), 683−687.
(18) Bai, S.; Tang, S.; Wu, M.; Luo, D.; Zhang, J.; Wan, D.; Li, X. Chromium ditelluride monolayer: A novel promising 2H phase thermoelectric material with direct bandgap and ultralow lattice thermal conductivity. *J. Alloys Compd.* **2023**, *930*, No. 167485.
(19) Bertolazzi, S.; Brivio, J.; Kis, A. Stretching and breaking of ultrathin MoS_2. *ACS Nano* **2011**, *5* (12), 9703−9709.
(20) Voiry, D.; Yamaguchi, H.; Li, J.; Silva, R.; Alves, D. C.; Fujita, T.; Chen, M.; Asefa, T.; Shenoy, V. B.; Eda, G.; Chhowalla, M. Enhanced catalytic activity in strained chemically exfoliated WS_2 nanosheets for hydrogen evolution. *Nat. Mater.* **2013**, *12* (9), 850−855.
(21) Hoffman, A. N.; Gu, Y.; Liang, L.; Fowlkes, J. D.; Xiao, K.; Rack, P. D. Exploring the air stability of $PdSe_2$ via electrical transport measurements and defect calculations. *npj 2d Mater. Appl.* **2019**, *3* (1), No. 50.
(22) Lupan, O.; Postica, V.; Hoppe, M.; Wolff, N.; Polonskyi, O.; Pauporte, T.; Viana, B.; Majerus, O.; Kienle, L.; Faupel, F.; Adelung, R. PdO/PdO_2 functionalized ZnO: Pd films for lower operating temperature H_2 gas sensing. *Nanoscale* **2018**, *10* (29), 14107−14127.
(23) Geng, X.; Li, S.; Mei, Z.; Li, D.; Zhang, L.; Luo, L. Ultrafast metal oxide reduction at Pd/PdO_2 interface enables one-second hydrogen gas detection under ambient conditions. *Nano Res.* **2023**, *16* (1), 1149−1157.
(24) Novoselov, K. S.; Fal'ko, V. I.; Colombo, L.; Gellert, P. R.; Schwab, M. G.; Kim, K. A roadmap for graphene. *Nature* **2012**, *490* (7419), 192−200.
(25) Cao, X.; Shi, J.-j.; Zhang, M.; Jiang, X.-h.; Zhong, H.-x.; Huang, P.; Ding, Y.-m.; Wu, M. Band Gap Opening of Graphene by Forming Heterojunctions with the 2D Carbonitrides Nitrogenated Holey Graphene, g-C3N4, and g-CN: Electric Field Effect. *J. Phys. Chem. C* **2016**, *120* (20), 11299−11305.
(26) Zhang, S. J.; Lin, S. S.; Li, X. Q.; Liu, X. Y.; Wu, H. A.; Xu, W. L.; Wang, P.; Wu, Z. Q.; Zhong, H. K.; Xu, Z. J. Opening the band gap of graphene through silicon doping for the improved performance of graphene/GaAs heterojunction solar cells. *Nanoscale* **2016**, *8* (1), 226−232.
(27) Mohanta, M. K.; Arora, A.; De Sarkar, A. Effective modulation of ohmic contact and carrier concentration in a graphene-MgX (X = S,Se) van der Waals heterojunction with tunable band-gap opening via strain and electric field. *Phys. Rev. B* **2021**, *104* (16), No. 165421.
(28) Wu, Y.; He, C.; Zhang, W. Building up a general selection strategy and catalytic performance prediction expressions of heteronuclear double-atom catalysts for N_2 reduction. *J. Energy Chem.* **2023**, *82*, 375−386.
(29) He, C.; Ma, J.; Wu, Y.; Zhang, W. Design of novel transition-metal-doped C_4N_4 as highly effective electrocatalysts for nitrogen fixation with a new intrinsic descriptor. *J. Energy Chem.* **2023**, *84*, 131−139.
(30) He, C.; Liang, Y.; Zhang, W. Design of Novel Transition-Metal-Doped C_6N_2 with High-Efficiency Polysulfide Anchoring and Catalytic Performances toward Application in Lithium-Sulfur Batteries. *ACS Appl. Mater. Interfaces* **2022**, *14* (25), 29120−29130.
(31) Zhang, W.; Hou, J.; Bai, M.; He, C.; Wen, J. Spontaneously enhanced visible-light-driven photocatalytic water splitting of type II PG/$AlAs_5$ van der Waal heterostructure: A first-principles study. *Chin. Chem. Lett.* **2023**, *34* (12), No. 108270.
(32) Kresse, G.; Furthmüller, J. Efficient iterative schemes for ab initio total-energy calculations using a plane-wave basis set. *Phys. Rev. B* **1996**, *54* (16), No. 11169.
(33) Kresse, G.; Joubert, D. From ultrasoft pseudopotentials to the projector augmented-wave method. *Phys. Rev. B* **1999**, *59* (3), No. 1758.
(34) Perdew, J. P.; Burke, K.; Ernzerhof, M. Generalized Gradient Approximation Made Simple. *Phys. Rev. Lett.* **1996**, *77* (18), No. 3865.
(35) Hummer, K.; Harl, J.; Kresse, G. Heyd-Scuseria-Ernzerhof hybrid functional for calculating the lattice dynamics of semiconductors. *Phys. Rev. B* **2009**, *80* (11), No. 115205.
(36) Zhang, Y. F.; Lin, W.; Li, Y.; Ding, K. N.; Li, J. Q. A theoretical study on the electronic structures of TiO_2: Effect of Hartree-Fock exchange. *J. Phys. Chem. B* **2005**, *109* (41), 19270−19277.
(37) Monkhorst, H. J.; Pack, J. D. Special points for Brillouin-zone integrations. *Phys. Rev. B* **1976**, *13* (12), No. 5188.
(38) Zhou, F.; Sadigh, B.; Åberg, D.; Xia, Y.; Ozoliņš, V. Compressive sensing lattice dynamics. II. Efficient phonon calculations and long-range interactions. *Phys. Rev. B* **2019**, *100* (18), No. 184309.
(39) Bengtsson, L. Dipole correction for surface supercell calculations. *Phys. Rev. B* **1999**, *59* (19), No. 12301.
(40) Klimeš, J.; Bowler, D. R.; Michaelides, A. Van der Waals density functionals applied to solids. *Phys. Rev. B* **2011**, *83* (19), No. 195131.
(41) Klimeš, J.; Bowler, D. R.; Michaelides, A. Chemical accuracy for the van der Waals density functional. *J. Phys.: Condens. Matter* **2010**, *22* (2), No. 022201.
(42) Thomas, M.; Brehm, M.; Fligg, R.; Vohringer, P.; Kirchner, B. Computing vibrational spectra from ab initio molecular dynamics. *Phys. Chem. Chem. Phys.* **2013**, *15* (18), 6608−6622.
(43) Banerjee, S.; Periyasamy, G.; Pati, S. K. Possible application of 2D-boron sheets as anode material in lithium ion battery: A DFT and AIMD study. *J. Mater. Chem. A* **2014**, *2* (11), 3856−3864.
(44) Nosé, S. A unified formulation of the constant temperature molecular dynamics methods. *J. Chem. Phys.* **1984**, *81* (1), 511−519.

https://doi.org/10.1021/acsomega.4c01305
ACS Omega 2024, 9, 28176−28185

(45) Liu, Q.-J.; Liu, Z.-T.; Feng, L.-P. Elasticity, electronic structure, chemical bonding and optical properties of monoclinic ZrO_2 from first-principles. *Phys. B* **2011**, *406* (3), 345−350.
(46) Chiu, M. H.; Zhang, C.; Shiu, H. W.; Chuu, C. P.; Chen, C. H.; Chang, C. Y.; Chen, C. H.; Chou, M. Y.; Shih, C. K.; Li, L. J. Determination of band alignment in the single-layer MoS_2/WSe_2 heterojunction. *Nat. Commun.* **2015**, *6* (1), No. 7666.
(47) Zhang, S.; Zhou, J.; Wang, Q.; Chen, X.; Kawazoe, Y.; Jena, P. Penta-graphene: A new carbon allotrope. *Proc. Natl. Acad. Sci. U.S.A.* **2015**, *112* (8), 2372−2377.
(48) Karak, S.; Bera, J.; Paul, S.; Sahu, S.; Saha, S. Low thermal conductivity and interface thermal conductance in SnS_2. *Phys. Rev. B* **2021**, *104* (19), No. 195304.
(49) Del Corro, E.; Botello-Mendez, A.; Gillet, Y.; Elias, A. L.; Terrones, H.; Feng, S.; Fantini, C.; Rhodes, D.; Pradhan, N.; Balicas, L.; Gonze, X.; Charlier, J. C.; Terrones, M.; Pimenta, M. A. Atypical Exciton-Phonon Interactions in WS_2 and WSe_2 Monolayers Revealed by Resonance Raman Spectroscopy. *Nano Lett.* **2016**, *16* (4), 2363−2368.
(50) Samad, A.; Shafique, A.; Kim, H. J.; Shin, Y.-H. Superionic and electronic conductivity in monolayer W_2C: ab initio predictions. *J. Mater. Chem. A* **2017**, *5* (22), 11094−11099.
(51) Beckstein, O.; Klepeis, J. E.; Hart, G. L. W.; Pankratov, O. First-principles elastic constants and electronic structure ofα−Pt_2Siand PtSi. *Phys. Rev. B* **2001**, *63* (13), No. 134112.
(52) Cui, H.; Jia, P.; Peng, X.; Li, P. Adsorption and sensing of CO and C_2H_2 by S-defected SnS_2 monolayer for DGA in transformer oil: A DFT study. *Mater. Chem. Phys.* **2020**, *249*, No. 123006.
(53) Zheng, H.; Zhang, J.; Yang, B.; Du, X.; Yan, Y. A first-principles study on the magnetic properties of nonmetal atom doped phosphorene monolayers. *Phys. Chem. Chem. Phys.* **2015**, *17* (25), 16341−16350.
(54) Wang, Y.; Li, Y.; Chen, Z. Not your familiar two dimensional transition metal disulfide: structural and electronic properties of the PdS2 monolayer. *J. Mater. Chem. C* **2015**, *3* (37), 9603−9608.
(55) Cao, K.; Feng, S.; Han, Y.; Gao, L.; Ly, T. H.; Xu, Z.; Lu, Y. Elastic straining of free-standing monolayer graphene. *Nat. Commun.* **2020**, *11* (1), No. 284.
(56) Liu, G.; Robertson, A. W.; Li, M. M.; Kuo, W. C. H.; Darby, M. T.; Muhieddine, M. H.; Lin, Y. C.; Suenaga, K.; Stamatakis, M.; Warner, J. H.; Tsang, S. C. E. MoS_2 monolayer catalyst doped with isolated Co atoms for the hydrodeoxygenation reaction. *Nature* **2017**, *9* (8), 810−816.
(57) Guo, Y.; Wang, F. Q.; Wang, Q. An all-carbon vdW heterojunction composed of penta-graphene and graphene: Tuning the Schottky barrier by electrostatic gating or nitrogen doping. *Appl. Phys. Lett.* **2017**, *111* (7), No. 073503.
(58) Devakul, T.; Crepel, V.; Zhang, Y.; Fu, L. Magic in twisted transition metal dichalcogenide bilayers. *Nat. Commun.* **2021**, *12* (1), No. 6730.
(59) Zhou, W.; Guo, Y.; Liu, J.; Wang, F. Q.; Li, X.; Wang, Q. 2D SnSe-based vdW heterojunctions: tuning the Schottky barrier by reducing Fermi level pinning. *Nanoscale* **2018**, *10* (28), 13767−13772.
(60) Padilha, J. E.; Fazzio, A.; da Silva, A. J. Van der Waals heterostructure of phosphorene and graphene: tuning the Schottky barrier and doping by electrostatic gating. *Phys. Rev. Lett.* **2015**, *114* (6), No. 066803.
(61) Mao, Y.; Xu, C.; Yuan, J.; Zhao, H. A two-dimensional GeSe/SnSe heterostructure for high performance thin-film solar cells. *J. Mater. Chem. A* **2019**, *7* (18), 11265−11271.
(62) Peng, Q.; Wang, Z.; Sa, B.; Wu, B.; Sun, Z. Electronic structures and enhanced optical properties of blue phosphorene/transition metal dichalcogenides van der Waals heterostructures. *Sci. Rep.* **2016**, *6* (1), No. 31994.
(63) Wu, Y.; He, C.; Zhang, W. Capture-backdonation-recapture" mechanism for promoting N2 reduction by heteronuclear metal-free double-atom catalysts. *J. Am. Chem. Soc.* **2022**, *144* (21), 9344−9353.
(64) Wu, Y.; He, C.; Zhang, W. Novel design strategy of high activity electrocatalysts toward nitrogen reduction reaction via boron−transition-metal hybrid double-atom catalysts. *ACS Appl. Mater. Interfaces* **2021**, *13* (40), 47520−47529.
(65) Hassan, A.; Nazir, M. A.; Shen, Y.; Guo, Y.; Kang, W.; Wang, Q. First-Principles Study of the Structural, Electronic, and Enhanced Optical Properties of SnS/TaS_2 Heterojunction. *ACS Appl. Mater. Interfaces* **2022**, *14* (1), 2177−2184.
(66) Nazir, M. A.; Shen, Y.; Hassan, A.; Wang, Q. The electronic and interfacial properties of a vdW heterostructure composed of penta-$PdSe_2$ and biphenylene monolayers. *Mater. Adv.* **2023**, *4* (6), 1566−1571.
(67) Hassan, A.; Guo, Y.; Wang, Q. Performance of the pentagonal PdSe2 sheet as a channel material in contact with metal surfaces and graphene. *ACS Appl. Electron. Mater.* **2020**, *2* (8), 2535−2542.
(68) Geim, A. K.; Grigorieva, I. V. Van der Waals heterostructures. *Nature* **2013**, *499* (7459), 419−425.
(69) Novoselov, K. S.; Mishchenko, A.; Carvalho, A.; Neto, A. H. C. 2D materials and van der Waals heterostructures. *Science* **2016**, *353* (6298), No. aac9439.
(70) Bruno, M.; Palummo, M.; Marini, A.; Del Sole, R.; Ossicini, S. From Si nanowires to porous silicon: the role of excitonic effects. *Phys. Rev. Lett.* **2007**, *98* (3), No. 036807.
(71) Uppstu, A.; Fan, Z.; Harju, A. Obtaining localization properties efficiently using the Kubo-Greenwood formalism. *Phys. Rev. B* **2014**, *89* (7), No. 075420.

https://doi.org/10.1021/acsomega.4c01305
ACS Omega 2024, 9, 28176−28185